2 Basics

In this introductory chapter, the physical background necessary for understanding the laser-induced phenomena encountered on the Gd(0001)/W(110) system is presented. After a description of the ferromagnetic Gd metal and the relationship between magnetism and electronic structure specific to this material, a brief introduction of the laser-induced electron dynamics is given. Furthermore, coherent lattice dynamics and the typical excitation mechanisms are reviewed. Ending this chapter, the optically induced magnetization dynamics together with the possible demagnetization pathways and the responsible elementary excitations involved, will be introduced.

2.1 Electronic structure and magnetism of gadolinium (Gd)

Gadolinium (Gd) belongs to the rare-earth elements that comprise the group of *lanthanides* metals from lanthanum (La) to lutetium (Lu). The common feature exhibited by the lanthanides is the successive filling of the $4f^n$ electron shell along the series: from $n=0$ for La to $n=14$ in Lu case. Under the rare-earth element term one usually includes also scandium (Sc) and yttrium (Y) [18, 19] although they have a different electronic configuration. The similarity with the rare-earth elements relies on the valence electronic structure. If the outer electronic shell occupancy is considered, one observes the analogy in electronic configuration between the lanthanides $(5d6s)^3$ and Y $(4d5s)^3$ and Sc $(3d4s)^3$ namely all are trivalent metals[1]. Since the conduction electrons are responsible for chemical bonding in the condensed matter phase one can consider [18, 19] these elements as being similar and thus can be included under rare-earth element notion.

Gadolinium is regarded [10] as the prototype of the localized magnetic moment ferromagnet due to its large magnetic moment confined at the core level. With its half-filled $4f$ shell Gd possess a magnetic moment of 7.63 μ_B per atom[2] [20] in solid state phase with the major contribution coming from the spin magnetic moment. Applying the Hund's rules to the $4f$ shell one obtains the maximum spin moment of S=7/2 and no orbital moment L=0. Since the $4f$ wave functions are strongly localized at the core level having a small overlap with the corresponding wave functions in neighboring atoms, there is a weak direct interaction among the $4f$ moments. Therefore, magnetic ordering on Gd and in general for lanthanides, is governed by the *indirect exchange interaction* or *RKKY interaction*[3] [21, 22, 23]. According to RKKY interaction, magnetic coupling of the $4f$ moments is mediated by the conduction electrons $(5d6s)^3$ and has an oscillatory spatial dependence. Thus, magnetically polarized conduction electrons contribute with the rest of 0.63 μ_B to

---

[1] In the case of lanthanides there are two exceptions: Eu and Yb that are divalent metals.
[2] The Bohr magneton μ_B is defined as $\mu_B = \frac{e\hbar}{m_e} = 9.274 \times 10^{-24} Am^2$
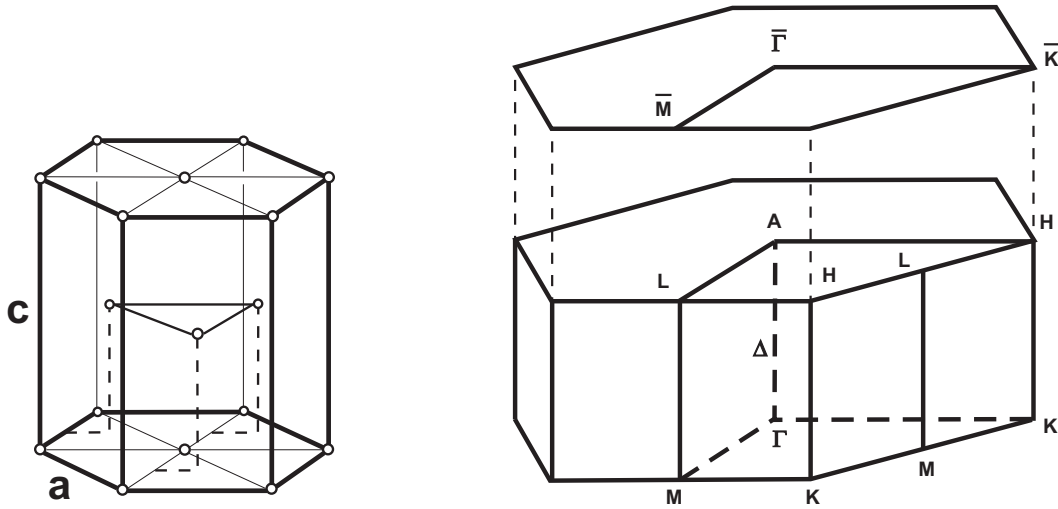[3] The acronym comes from the name of the authors Ruderman, Kittel, Kasuya, Yosida.

Figure 2.1: Left: the hexagonal closed-packed (hcp) unit cell for gadolinium together with the respective lattice parameters. The size of the atoms is arbitrary. **Right**: the corresponding bulk and surface Brillouin zones of the hexagonal lattice showing the high symmetry directions and points.

the total magnetic moment of Gd, this contribution having an itinerant character. As a remark, in general for the rare earth metals, the 4f magnetic moments retain their atomic value also in the solid state phase. This is such because the orbital momentum contribution to the total magnetic moment is not quenched by the crystal field (which is the case for *3d* ferromagnets Ni, Fe, Co) due to the "screening" realized by the closed shells electrons $5s^2 5p^6$.

The localized-moment magnetism picture is well described in the framework of the Heisenberg model by the hamiltonian operator having the following form:

$$H = -\sum_{i,j} J_{ij}(\mathbf{r}_{ij}) \mathbf{S}_i \mathbf{S}_j \qquad (2.1)$$

where $\mathbf{S}_i$ and $\mathbf{S}_j$ are the spin moments positioned on two neighbor atomic sites at a distance r_{ij} that are coupled together by the exchange interaction constant J_{ij}. Classically, the above expression can be understood in terms of a effective magnetic field $B_{eff} \sim J_{ij} S_i$ *i.e.* the exchange field, created by the spin moment $\mathbf{S}_i$ that is exerted on the neighbor spin $\mathbf{S}_j$. Therefore, depending on the sign of the J_{ij} either a parallel or antiparallel spin alignment take place, which means a ferromagnetic or antiferromagnetic ordering is favored, respectively.

In the lanthanides serie Gd has the highest magnetic ordering temperature of T_c= 293K and is the only element that exhibits a simple ferromagnetic to paramagnetic phase transition without an intermediate antiferromagnetic ordering. This is the reason why Gd together with the transition metals ferromagnets (Ni, Fe, Co) is considered as a "classical" ferromagnet.
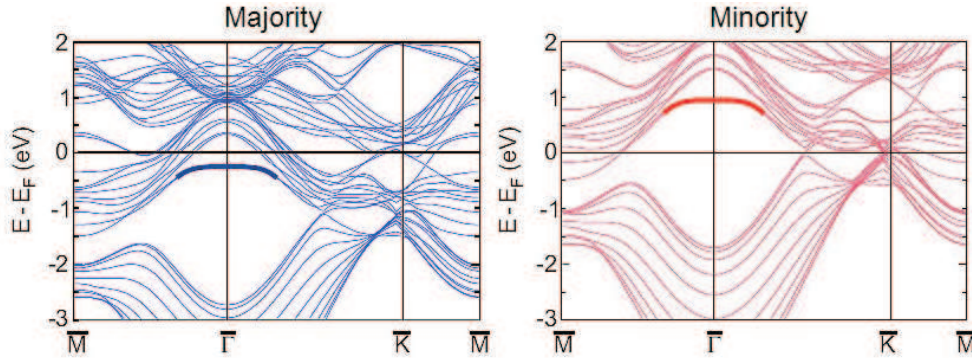
Figure 2.2: Calculated spin-resolved band structure for ferromagnetic Gd(0001) surface within local density approximation (LDA) theory. The surface state components are depicted by the thick lines in the band gaps of the majority and minority band structure. Note, that the energetic position of the minority surface state is not coinciding with the experiment. From [26].

Gadolinium crystallizes in a hexagonally closed-packed structure (hcp), a structural symmetry that it is retained also for epitaxially grown thin films on W(110) substrate [24]. The hcp unit cell together with the corresponding bulk and surface Brillouin zones showing the high symmetry points and directions are depicted in the figure 2.1. The lattice parameters for Gd are a=3.629Å and c=5.796Å [25] ($c/2$=2,89Å defines one monolayer (ML) of gadolinium).

Particular for the Gd electronic structure at the (0001) surface is the presence of Tamm-like surface state in the band-gap of the projected bulk band structure. It arises from the 5d bulk bands and spatially it is strongly localized in all three directions. This can be seen from the calculated band structure for ferromagnetic gadolinium in figure 2.2 where the surface state exhibits almost no dispersion along $k_{\parallel}$ direction. The d_{z^2}-like orbital symmetry of the surface state depicted in figure 2.3, presents a charge distribution that is positioned at the atomic site having 89% of the charge confined in the topmost layer of Gd surface [27]. Energetically, the surface state resides around the Fermi level with an occupied component having majority spin character and an unoccupied one with minority spin orientation[4] (at T=0 K) [29, 30]. The energetic separation between surface state components, is denoted as *exchange splitting* (Δ_{ex}) and reflects the degree of magnetic ordering of the system. It was shown that in the case of magnetically ordered lanthanides the zero-temperature (or very low temperature exchange T=10 K) splitting scales with the magnitude of the $4f$ moment [31, 30].

The electronic structure of Gd and in particular the surface state received a lot of attention from both theory and experiment in order to clarify what is the mechanism that governs the magnetic ordering at elevated temperatures. This was a controversial issue over the past years. Various investigation techniques were involved like photoemission, inverse photoemission that access the occupied and unoccupied electronic structure,

---

[4]The surface state components have a pure majority or minority spin character at T=0 K, for higher temperatures the states being spin-mixed [28].
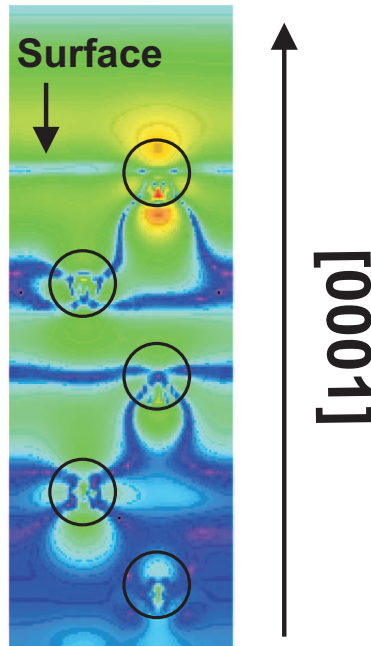
Figure 2.3: Charge density map of the majority surface state electrons of ferromagnetic gadolinium along [0001] direction. The low density areas are depicted in blue whereas the high density regions are showed in red. The map shows a section through five atomic layers with the atoms sites depicted by the empty circles. The location of the surface plane is indicated by the arrow. Note the d_{z^2} orbital symmetry of the surface state and the distribution of charge that is mostly localized in the first atomic layer. Adapted from [26]

respectively, and scanning tunnelling spectroscopy (STS) that probes both parts in the vicinity of Fermi level. A number of studies reported a decrease of the exchange splitting with increasing temperature and a collapse at the Curie point [32] while others showed a similar temperature dependence in the ferromagnetic phase but a non-zero Δ_{ex} at T_C and above [33, 34]. Also the existence of an enhanced surface Curie temperature determined by the presence of the surface state and/or the lower atomic coordination number in the surface layer was a matter of debate. This latter issue was settled by the group of Pappas [35] by demonstrating an identical T_C of Gd surface with the bulk. Regarding the exchange-split electronic states, now the common believe is that for both the surface state and the $5d$ bulk states the exchange splitting remains finite and constant at T_C while the spin polarization is lost [33, 36].

More detailed, the exchange splitting of the surface state varies with temperature from 0.7 eV at 10 K to a constant value of 0.4 eV at Curie point and above [33] (up to the highest investigated temperature of 360 K). These observations are also confirmed by the measurements reported in this thesis (see chapter 5), in which we could probe the spin polarization and the exchange splitting of the surface state by employing magnetization-induced second harmonic generation (MSHG) and two-photon photoemission (2PPE) techniques[5],

---

[5]The MSHG and 2PPE techniques are described in chapter 3 and chapter 5, respectively.
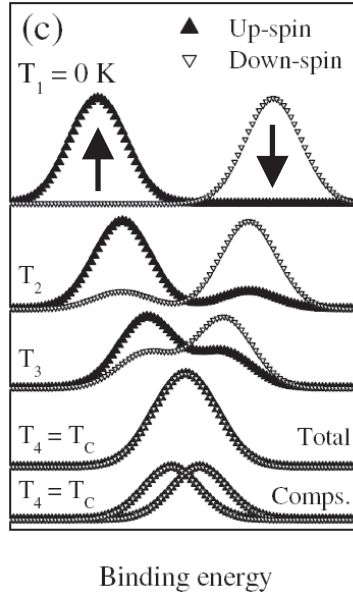
Figure 2.4: Qualitative illustration of the temperature-dependent scenario of the $5d$ states on Gd(0001) that includes spin-mixing and Stoner-like behavior. The spin orientation is indicated by the arrows. At T=0 the exchange splitting is finite and there are no spin-mixed states. Increasing the temperature the Δ_{ex} decreases while the amount of spin-mixing increases. At T_C the spin polarization of the states is zero whereas the exchange splitting does not vanish, denoted by the last two instances in the figure, respectively. From [36].

respectively. A similar temperature-dependent behavior was recently reported also for the delocalized *5d* bulk bands [36] with the distinction that at low temperature the exchange splitting is slightly larger than at the surface with ≈ 0.8 eV.

Magnetism on Gd at finite temperatures: Stoner versus spin-mixing behavior

On a microscopic level, the ferromagnetic order in solids at finite temperatures is explained in the framework of two different models, *Stoner* [37] and *spin-mixing* [10] model, which predict the mutual relationship of magnetism and electronic structure. These models are idealized pictures that treat the origin of magnetic ordering according to the degree of localization of the electrons that carry the magnetic moments. On one side is the Stoner model that describes the itinerant electron systems like Ni, Fe, Co and on the other side is the spin-mixing model based on the Heisenberg model that accounts for the magnetism of the localized electrons. In the Stoner picture the exchange splitting varies with temperature in ferromagnetic phase and collapses to zero in paramagnetic phase reflecting the M(T) behavior, whereas for the spin-mixing model Δ_{ex} is temperature independent with the magnetization decrease explained by fluctuation and excitation of the localized magnetic moments.

As was shown above, for the localized surface state and the delocalized *5d* bands, the exchange splitting varies with temperature exhibiting no collapse at the critical temperature

and higher, although the long-range magnetic order is lost. These results are surprising since one might think that the delocalized states are sensitive to the long-range magnetic ordering, *i.e.* average magnetization of the sample, which is lost in the paramagnetic phase. On the other hand, the surface state due to its localization is sensitive to the local magnetic ordering *i.e.* on-site magnetic moment whose magnitude is conserved with regard to temperature variations. Hence, one could expect that the delocalized states to resemble a Stoner-like behavior while the localized ones to behave according to the spin-mixing scenario.

Therefore, it was concluded that neither the Stoner model nor the spin-mixing picture is suitable to describe the magnetic properties of Gd at finite temperatures. Although initially unexpected, the dependence of Δ_{ex} on temperature is rather a complex interplay between Stoner-like (delocalized) behavior and the spin-mixing (localized) behavior.

Such a scenario, which can be considered as the closest picture to the reality, is illustrated in the figure 2.4 where temperature evolution of the exchange-split *5d* bulk states is presented. At T=0 K the majority and minority sub-bands have a well defined exchange splitting and show no spin mixed states. Increasing the temperature the exchange splitting is reduced and a significant amount of spin mixing (also referred to as spectral weight transfer) is taking place. At the Curie point the spin polarization becomes zero while the separation in energy of the spin up and spin down states is still observable *i.e.* a non-vanishing exchange splitting remains at T_C.

2.2 Laser-induced electron dynamics

In this section the general features of the laser-induced electron dynamics in metals are described in order to provide a knowledge base for understanding the encountered ultrafast phenomena on Gd(0001) and Y(0001) presented in chapter 5 and 6, respectively.

2.2.1 Absorption of light in metals

Assuming average incident intensities, the absorption of light in solid materials is governed by the Lambert-Beer's law

$$I(d) = I_0 exp[-\alpha(\omega)d] \tag{2.2}$$

which gives an exponential spatial profile of the intensity within the material[6]. The optical properties of the material enter in the above equation through the absorption coefficient α (sometimes is called also extinction coefficient). This renders the spatial extent over which the light is absorbed namely the *optical penetration depth* or the *skin depth δ* [7] which is defined as follows:

$$\delta = \frac{\lambda}{4\pi k} = \alpha^{-1} \tag{2.3}$$

where λ is the light wavelength and k is the imaginary part of the complex refractive index $\widetilde{n}$=n+ik. In the case of metals, the optical penetration depth for laser wavelengths in the

---

[6]Equation 2.2 is correct in the assumption that multiple reflections and scattering within the material are neglected.

[7]The penetration depth for the electric field amplitude is $\delta = \frac{\lambda}{2\pi k}$
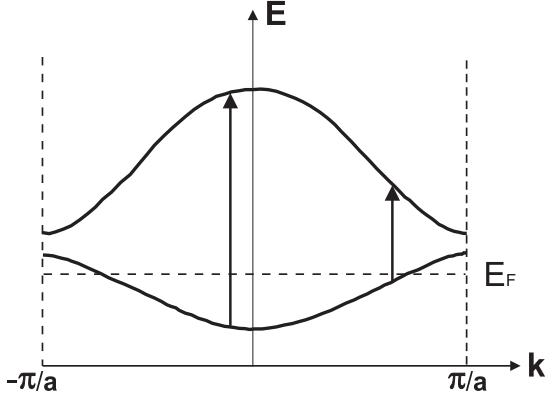
Figure 2.5: The laser-induced vertical optical transitions (arrows) with different photon energies in a generic band structure (within the first Brillouin zone) of a metal.

visible spectral range varies between $10 - 30$ nm. As a remark, the exponential spatial profile of the absorbed intensity within material leads to an inhomogeneous excitation profile. The gradient in the absorbed energy density determines the transport of the photo-injected energy out of the detection region by ballistic or/and diffusive transport by non-equilibrium or/and thermalized electron population, respectively. These transport effects are detailed in the next section.

In a quantum mechanical approach the absorption coefficient α is given by the transition rate $W_{i \to f}$ of exciting an electron between initial Ψ_i and final Ψ_f quantum state upon absorption of a photon:

$$W_{i \to f} = \frac{2\pi}{\hbar}|M_{if}|^2 \delta(E_f - E_i - h\nu) = \frac{2\pi}{\hbar}|\langle f|H|i\rangle|^2 \delta(E_f - E_i - h\nu) \tag{2.4}$$

where $M_{if} = |\langle f|H|i\rangle| = \int \Psi_f(r)H(r)\Psi_i(r)d^3r$ represents the transition matrix elements involving the perturbation hamiltonian $H(r)$ that describes the interaction of the optical wave with the electron of coordinate r. Within electric dipole approximation the perturbation hamiltonian reads $H(r) = \frac{e}{2m_e c}(\mathbf{A} \cdot \mathbf{p} + \mathbf{p} \cdot \mathbf{A})$ with $\mathbf{p}$ and $\mathbf{A}$ being the momentum operator and the vector potential of the incident electromagnetic wave, respectively. The δ-Dirac function determines the energy conservation. The latter quantity is available for transition between discrete energetic levels *e.g.* for atoms or molecules. For solids this should be replaced by the joint density of states $g(h\nu)$ given by the convolution of the initial and final states of the optical transition. The momentum conservation condition reads:

$$\hbar\mathbf{k}_f - \hbar\mathbf{k}_i = \hbar\mathbf{k} \tag{2.5}$$

Since the photon wavevector $|\mathbf{k}| = \frac{2\pi}{\lambda}$ for optical frequencies is negligibly small compared to the electron wavevectors that have characteristic size of the Brillouin zone π/a, where a is the lattice constant, one can write eq 2.5 as:

$$\mathbf{k}_f = \mathbf{k}_i \tag{2.6}$$

The latter equation shows why an optical transition is represented by a vertical arrow in the E($\mathbf{k}$) diagram, as can be seen in the figure 2.5.

2.2.2 Optical excitation and relaxation of electrons in metals

Collective electron dynamics

Initially, the absorption of a femtosecond laser pulse of energy $h\nu$ takes place into the limit of the optical penetration depth δ and produces a coherent collective polarization of the electron population. This induced electronic polarization has an oscillatory behavior and preserves the optical phase memory of the exciting laser pulse. Subsequently (on a < 10 fs time scale after excitation[8]), the collective electron motion decays via phase destructive events like electron-electron, electron-thermal phonons or electron-defect scattering. These processes have an elastic character *i.e.* the electrons retain their kinetic energy but the phase coherence is lost, which means the momentum is randomized. Therefore the initially deposited energy into the system is dissipated by creating an highly excited ensemble of incoherent electron-hole pairs which do not obey the Fermi-Dirac statistics. The resulting non-Fermi distribution is depicted in the top part of the figure 2.6, which sketches its rectangular shape whose dimensions are determined by the energy of the exciting laser pulse $h\nu$ and the absorbed energy density.

Electronic thermalization

Subsequent to the dephasing of excited electron-hole plasma, within the electron system, that is still in a highly non-equilibrated state, a redistribution of the excess energy carried by the optically excited conduction electrons occurs. This process known as the electronic *thermalization* proceeds through inelastic electron-electron scattering.

Depending on the excitation density one can distinguish two regimes for the photoexcited electron dynamics:

- the *low excitation* density ($< 10^{-3} e^-/$atom) determines a single-electron dynamics where the single excited electron interact with the "cold" electrons situated at and below the Fermi level.

- the *high excitation* density ($> 10^{-3} e^-/$atom) where one encounters an excited electronic ensemble that will be internally equilibrated by scattering of the excited electrons among themselves.

For the low excitation density regime the scattering rate and thus the lifetime of the excited single-electrons can be deduces within the framework of Landau's Fermi-liquid theory (FLT) [38, 39, 40] which predicts (for a three-dimensional free electron gas at T=0 K):

$$\tau_{e-e} = \tau_0 \frac{1}{(E - E_F)^2} \tag{2.7}$$

$$with \qquad \tau_0 = const \cdot n^{\frac{5}{6}} \tag{2.8}$$

From here we notice that the electronic lifetime τ_{e-e} depends on the excess energy of the excited electron with respect to Fermi level and on the density of the electron gas

---

[8]One way to investigate this nascent electron dynamics is to employ nonlinear autocorrelation techniques involving ultra-short laser pulses.
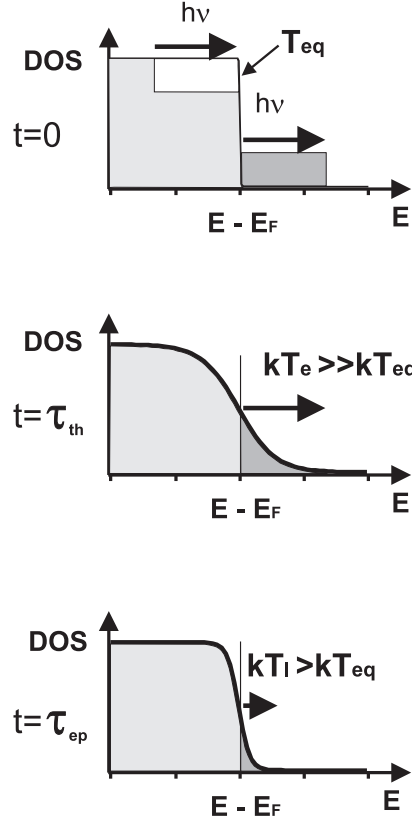
Figure 2.6: The laser excitation and the subsequent transient electron dynamics. **Top**: At t=0 the pump pulse excite the electron gas that exhibits a non-Fermi rectangular distribution given by the absorbed energy density and the photon energy $h\nu$. BEfore excitation the system is characterized by a temperature T_{eq}. **Middle**: The highly excited non-equilibrium electrons thermalize within a typical time τ_{th} around a few 100 fs, through e-e scattering to a Fermi-Dirac distribution of hot electrons characterized by temperature T_e. **Bottom**: Through e-p scattering the energy is transferred from electron to the phonon bath and eventually their temperatures equalize $T_e = T_l$.

n. In other words the lifetime of excited electrons depends on the available *phase space* to scatter *i.e.* the number of scattering partners and the available amount of final states for scattering. On one hand, higher the excess energy interval higher is the number of achievable final states that increase the scattering probability and the electronic lifetime becomes smaller. On the other hand, a higher electron density n increases the phase space for scattering but in the same time the Coulomb interaction is reduced due to the reduced screening length and thus reducing the scattering probability and increasing the electronic lifetime. Thus there is the competition between these two effects that gives the final lifetime of the excited electrons.

A relatively good agreement between FLT and experiment was found for electronic lifetimes measured on silver and tantalum [40, 41]. However, a consistent deviation for transition metals Fe, Co, Ni [42, 41] was measured. The authors ascribed this behavior to

larger phase space to scatter in the case of transition metals determined by the unoccupied d states. For Ag the d states are completely filled and localized well below E_F and therefore just the s-p states play a role in the relaxation of excited electrons. This explains its behavior as a free-electron metal (*i.e.* one of the basic assumptions of the FLT) and the concordance with FLT prediction.

For finite temperatures the accurate description of the electronic lifetime is given by [39]:

$$\tau_{e-e}^{-1} = 2\beta[(\pi k_B T)^2 + (E - E_F)^2] \tag{2.9}$$

where β denotes the probability of $e-e$ scattering and thus reflecting also the screened Coulomb interaction. However, the temperature-dependent term in eq. 2.9 is usually neglected since at low temperature has a small value while at higher temperatures the contribution from e-p scattering is dominant. However, on the ultrafast time scales when the electron temperature reaches a few 1000 K (see fig. 2.7), while the lattice is relatively cold, the e-e lifetime has a T^2 dependence given by the first term in the above equation.

For the high excitation density regime the electron-electron scattering among the optically excited electrons results in a Fermi distribution of "hot" electrons characterized by an electronic temperature T_e. The electron-electron collisions produce cascades of secondary electrons with energies close to Fermi level[9]. Electronic temperatures T_e in order of a few 1000 K can be achieved before a significant energy transfer due to coupling to phonons can occur. These high electronic temperatures are developed due to small heat capacity of the electronic system compared to phonons.

The inhomogeneous excitation within the absorption profile of the laser pulse results in a spatial energy gradient which is the source of efficient transport effects that dissipate the energy out of the excited region. The transport effects are competing with e-e and e-p scattering events that redistribute the photo-injected energy within the excited region. On the time scale of non-equilibrium electrons (<100 fs), there is the so-called *ballistic transport*, that evolves at Fermi velocity [43] *i.e.* v$\approx 10^6$m/s, the energy can by rapidly distributed over large distances (*e.g.* 100nm for Au [44]) to deeper, unexcited regions of the sample.

Electron-phonon scattering and the two-temperature model

After the thermalization of the electron bath, there still exists a thermal non-equilibrium between the electrons and the lattice. In the following few picoseconds (the typical time scale for metals), the electrons excite phonons and therefore an energy exchange with the lattice is taking place until the temperature of the electron system and the lattice equalize. The hot electrons loose their energy to the phonon bath by electron-phonon coupling, the strength of the coupling between those baths governing the time interval on which the energy transfer evolves.

In a simple picture, the electron-phonon interaction can be seen as the local distortion of the lattice produced by a phonon that affects in turn the local electronic structure

---

[9]Secondary electrons are low energy electrons produced in cascade and Auger-like events. During these processes, the optically excited electrons release their energy to the electrons situated initially below E_F that are promoted on higher unoccupied energy states in the vicinity of E_F.
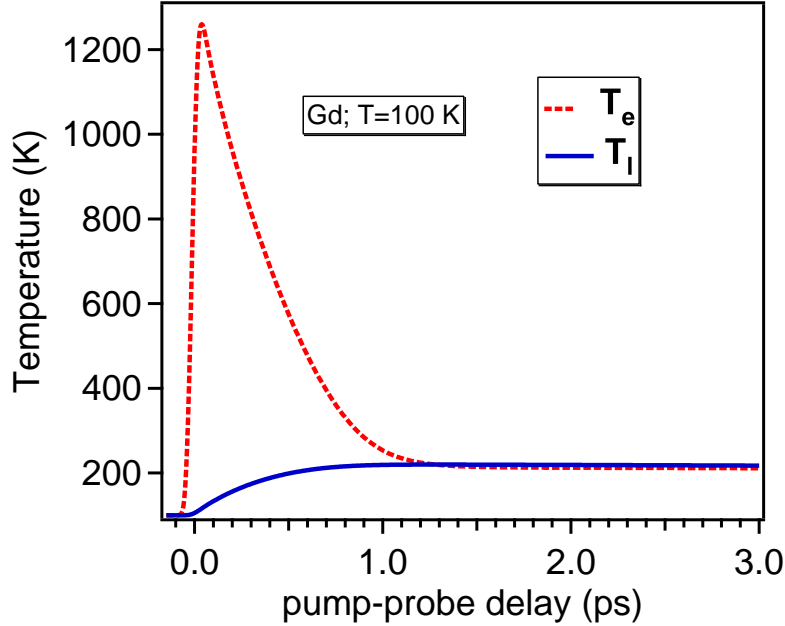
Figure 2.7: The calculated temperature transients according to 2TM model [45] of the electron T_e (dashed line) and phonon T_l (solid line) bath for a 20 nm gadolinium thin film upon laser excitation at a fluence of 0.5 mJ/cm^2. The initial static temperature of the system was 100 K. Note the relatively high electronic temperature of $\approx$1200 K and the equilibration with the lattice in 1 ps time scale. The used parameters are displayed in table 2.1.

or vice-versa as a travelling electron that polarizes the local environment and produce a distortion of the lattice (polaron picture). The effect of the electron-phonon interaction is reflected by a modified electron effective mass.

Microscopically, the essence of the *e-p* interaction resides in the fact that a phonon of energy $\hbar\Omega$ might be created or annihilated during the interaction. The evaluation of the electron-phonon scattering rate and implicitly the lifetime can be done within the Debye model according to the equation [46]:

$$\tau_{e-p}^{-1} = \frac{2\pi\lambda k_B T}{\hbar} \tag{2.10}$$

where λ is the electron-phonon mass enhancement factor and k_B is Boltzmann constant. λ gives the strength of the coupling between the electron and phonon bath, which contributes (besides interaction with other quasiparticle *e.g.* magnons) to the electron mass renormalization as $m_{eff} = m(1+\lambda)$. Here m is the mass of a non-interacting electron. The validity of the above equation has been shown to hold [47, 48] for temperatures $T > \Theta_D/3$ where Θ_D is the Debye temperature of the system. The linearity between the electron-phonon scattering rate and temperature is determined by the number of the thermally excited phonons that increase linear with temperature, and thus the resulting *e-p* scattering rate exhibiting the same behavior with respect to T dependence. As a remark, the

15

Property	Value
e-p coupling (g) [W/m^{3}K] [50]	$2.5 \cdot 10^{17}$
electron heat capacity (γ) [J/m^{3}K^2] [51]	225
electronic heat conductivity (K_e) [W/mK] [52]	11
penetration depth [nm] (at 800 nm)	20
Debye temperature (Θ_D) [K] [53]	163

Table 2.1: The physical properties used in the 2TM simulation for Gd at a temperature of 100 K and incident laser pulse of 50 fs duration.

e-e scattering prevails over *e-ph* scattering in the low temperature range and vice-versa for higher temperatures. This point is important in the view of investigating the possible decay channels of elementary excitations on ferromagnetic Gd, as will be presented in chapter 5.

At this stage, there is an additional mechanism of energy redistribution of the hot electron bath namely the *electron diffusion* process. This is determined by the temperature gradient in the sample and its efficiency is governed by the electron-phonon coupling.

Both relaxation mechanisms are included in a model that describes the energy transient in time and space between electron and the phonon baths: the *two temperature model* (2TM). Proposed for the first time by Anisimov [49], the model assumes that the electrons and lattice are in a local thermal equilibrium, and the energy transfer is determined by a set of coupled differential equations having the following form:

$$C_e(T_e) \cdot \frac{\partial T_e}{\partial t} = \frac{\partial}{\partial z}\left(K_e \frac{\partial T_e}{\partial z}\right) - g \cdot (T_e - T_l) + S(z,t)$$

$$C_l \cdot \frac{\partial T_l}{\partial t} = g \cdot (T_e - T_l)$$

$$(2.11)$$

Here $C_e = \gamma T_e$ (γ is a constant related with the density of states at the E_F) and C_l denote the electronic and lattice heat capacities, K_e is the electronic thermal conductivity and common term g is the electron-phonon coupling constant that gives the energy transfer rate per unit volume between electrons and phonons. The source term $S(z,t)$ is dependent on the optical properties of the system through the optical skin depth and gives the initial excitation depth profile.

$$S(z,t) = (1 - R - T)I_0 \alpha e^{-z\alpha} e^{-(\frac{t}{\tau})^2} \qquad (2.12)$$

where R and T represent the reflected and transmitted parts from the incident intensity I_0, respectively, and τ is the laser pulse duration.

Since the model treats the electron bath as being already internally equilibrated, does not provide information about the electronic nascent dynamics. This apparent drawback can be circumvented by employing extended variants of the 2TM that account for the non-equilibrated electron distribution [54, 55, 56].

Thermal diffusion

After the temperature equilibration of the electron and phonon baths, the thermal gradient existent in the system determines the cooling of the laser heated regions according to the classic heat diffusion equation:

$$K \cdot \nabla^2 T + C \cdot \frac{\partial T}{\partial t} = \frac{\partial U}{\partial t} \qquad (2.13)$$

with K thermal conductivity, U the heat per unit volume and C the heat capacity per unit volume. The thermal gradient is determined partially by the laser absorption profile and the possible energy redistribution through ballistic and diffusive electron transport. Usually the thermal diffusion is ignored in the frame of the 2TM model since it evolves on hundreds of picosecond time scale, which is not of interest for the *e-p* temperature equilibration (few picoseconds time scale). The initial temperature of the system, before laser irradiation, will be therefore recovered on a nanosecond to microsecond time scale plus a small increase dependent on the system's heat capacity and the laser repetition rate.

2.3 Electron-magnon scattering

Beside the above mentioned scattering mechanisms that dissipate the optically injected energy into the system, another decay channel should be considered in the case of ferromagnetic materials. This is the *spin-wave* or *magnon* bath which can accommodate some part of the excess energy carried initially by electrons. The energy transfer is driven here by electron-magnon (*e-m*) coupling with the efficiency of the energy redistribution depending on the coupling strength.

As for the case of electron-phonon coupling where the electron polarizes the lattice and vice-versa, also the electron-magnon coupling can be viewed as an electron of a certain spin orientation that magnetically polarizes the surrounding electrons with the opposite spin, that compensates its spin. Quantum-mechanically the magnons are excited by spin-flip events which reduce the magnetic moment along the quantization axis of the system.

The *e-m* coupling was shown to be comparable or even higher than the electron-phonon coupling in the case of Gd [57, 58]. Therefore it is playing an important role in the overall energy redistribution in the system and consequently in the magnetization dynamics on this material.

In the early measurements performed to determine the heat capacity of ferromagnetic materials, the signature of the electron-magnon interaction was identified from the additional term to the total measured heat capacity of the system which should be accounted for in order to have a good description of the measured data [59, 60]. More recently, photoemission investigation of the surface electronic structure on Gd(0001)/W(110) [28] and on Fe(110)/W(110) [61] systems showed a considerable contribution of *e-m* scattering to the decay of photoexcited surface state electrons. Interestingly, a consistent electron-magnon weight to the total decay rate was found mainly for minority (spin down) electrons channel. This last point was also supported by theoretical work of Zhukov *et al.* [62] for

the case of Fe and Ni, which shows a bigger contribution of spin-flip scattering rate[10] to the decay in the minority channel with respect to the majority one and therefore different lifetimes. The difference in the lifetimes for different spin orientation in $3d$ metals was ascribed to the restricted phase space for scattering in the spin-up channel with regard to spin-down component *i.e.* the available density of states (DOS) above E_F (mainly the d band) for minority electrons.

In order to account for the spin dependent lifetimes for the Gd surface, a calculation in the framework of the *s-f* model[11] was performed [63], which gives the following relation for the lifetime of the minority component:

$$\frac{1}{\tau_{e-m}^{\downarrow}} = \frac{\sqrt{3}}{4} \frac{p(\uparrow)m^*}{\hbar S} \left(\frac{2JSa}{\hbar}\right)^2 \qquad (2.14)$$

where $p(\uparrow)$ is the spin-up relative contribution to the spin-down state written in terms of electronic polarization, m^* is the effective mass in the surface band, J is the exchange interaction, S is the spin moment and a is the lattice constant. The basic decay mechanism invoked in the model is the electron spin-flip scattering with emission or absorption of magnons. From the above relation one can see that the electron-magnon scattering time for a certain spin orientation scales inversely with the number of electrons of opposite spin p and the exchange splitting *2JS*. Thus, the above equation relies also on the phase space related lifetimes since the polarization represents the electronic population and the exchange splitting is giving actually the amount of spin-mixed states where the electrons can scatter. The lifetime of majority electrons can be determined with the same relation 2.14 by including $p(\downarrow) = 1 - p(\uparrow)$.

Since the magnons represent low-energy excitations of the magnetic system, they can couple or even can be excited by the thermal excitations of the lattice that are in the same energy range. Therefore, increasing the temperature of the system the *e-m* scattering will increase but in the same time also the *e-p* scattering will grow due to higher magnitude of the thermal background. Hence, for the particular case of Gd, the decay rate of excited electrons, at higher temperatures, will be governed by the sensitive balance between *e-m* and *e-p* scattering events, whose strengths are comparable according to literature [57, 58].

Another process that involves the reversal of electron spin is the so-called *Stoner excitation* [37] that describes an electron-hole pair with opposite spins *i.e.* the promotion of a spin up (down) electron in the spin-down (up) sub-band leaving behind a hole in the occupied band. Thereby one electron can flip its spin by absorbing or releasing an energy amount equal with the exchange splitting of the corresponding band. For the case of Gd(0001) the exchange splitting of the conduction band amounts to 0.7 eV whereas for the $4f$ electrons is around 11 eV, which results in a low probability of these processes. Thus, the Stoner excitations provide a direct and fast relaxation channel between the electron and the spin baths and also an energy exchange mechanism between majority and minority sub-bands.

---

[10]Spin-flip scattering represents the e-e scattering in which the electrons involved change their spin orientation. Any spin-flip event requires the emission or absorption of a quasiparticle *e.g.* magnon or phonon in order to conserve momentum.

[11]The *s-f* model or Kondo-lattice model describes the interaction of the localized 4f electrons possessing a spin moment S with the itinerant 5d6s conduction electrons via an interband exchange interaction J.

Summarizing, the electron-magnon scattering is one important decay channel in the case of ferromagnetic systems, and depending on its strength may play an essential role in the laser induced demagnetization dynamics, as will be shown in chapter 5.

2.4 Coherent lattice dynamics

In the previous section we have identified different stages in the time evolution of the excitation and relaxation of the electron population in metallic systems upon an ultrashort laser pulse irradiation. The initial deposited energy in the system was redistributed to electron, phonon and magnon baths by inelastic collision events like *e-e*, *e-p* and *e-m* scattering resulting in an incoherent dynamics of the involved quasiparticles. Beside these incoherent phenomena, another type of effects might appear upon laser photoexcitation since the equilibrium between the electrons and the lattice is dramatically disturbed. These are lattice vibrations that posses a high degree of spatial and temporal coherence, the so-called *coherent phonons*. The generation and relaxation of coherent *optical* phonons will be the topic of the following section, with special attention being devoted to the excitation mechanisms. The physics of the *acoustic* phonon modes generated by lattice heating following the laser excitation together with a theoretical model that describes their excitation and temporal evolution, will be addressed in chapter 6.

2.4.1 Coherent phonon generation and detection

Coherent lattice vibration in THz frequency range were observed on various materials such as bulk insulators, semiconductors, semi-metals and superconductors being investigated in time domain with linear and nonlinear optical methods and in frequency domain by Raman scattering. Until very recently [17, 64] there was no report about coherent optical phonons measured on metals. This might be related with the ultrafast screening of the excited carriers by the surrounding electron bath, which results in a less effective driving term (eq. 2.17) for the phonon excitation. *Actually, the measurements performed on Gd(0001) presented in this thesis, are the first time reported coherent optical phonons on a metallic material.* A thoroughly description of this new observed phenomenon is given in chapter 5.

One of the main ingredients of coherent phonon generation is the laser pulse duration, which should be shorter than the period of the excited lattice vibration. This condition is usually fulfilled employing femtosecond laser systems that can deliver pulses down to 10 fs duration, since the eigenfrequencies of the phonon optical modes lie in the range of a few THz *i.e.* an oscillation period of several hundreds of femtoseconds. The example of the observed coherent phonons on Gd(0001) surface [17] (see figure 5.21) is eloquent here with an oscillation frequency of 3 THz that corresponds to a period of 330 fs.

Historically, there are two types of excitation mechanisms that are considered for the generation of coherent optical phonons: the *impulsive stimulated Raman scattering (ISRS)* [65] and *displacive excitation of coherent phonons* (DECP) [15]. The former one is thought to be responsible for lattice vibrations in transparent materials whereas the latter one is employed for absorbing media. As one can readily see from these limitations, the ISRS

mechanism involves the nonlinear process of phonon generation in the electronic ground state by a Raman process while the DECP is related with an excited electron population upon laser pulse absorption. Both excitation mechanisms are sketched in figure 2.8.

In the case of ISRS, the excitation of coherent phonon population is realized via the inelastic Raman scattering process, and produces the ions oscillation in the ground state around the equilibrium nuclear coordinate Q_0 (see upper part of the figure 2.8). The energy of the coherent phonon $\hbar\Omega$ is given by the energy difference between the two photons involved in the inelastic Raman process, whom energies $h\nu$ and $h\nu_1$ are covered by the spectral bandwidth of the exciting femtosecond laser pulse. Also phonons with wavevector $q \neq 0$ can be generated according to momentum conservation by choosing different angles of incidence for the two incident photons. This fact constitutes an advantage of this excitation model.

Regarding the DECP mechanism, the excitation of the electronic system will quasi-instantaneous (on the time scale of laser pulse duration) change the electron-ion potential *i.e.* screening of the Coulomb repulsion of the ions is less effective and therefore a new equilibrium separation is established. Accordingly, the system will evolve on a new potential energy surface with the minimum position Q^* displaced with respect to the initial ground state minimum coordinate Q_0 (see lower part of the figure 2.8). This will set an in-phase oscillatory motion of the ions around the new equilibrium position.

One way to distinguish between the excitation mechanisms is to account for the initial phase of the detected oscillations (see figure 2.8): there is a sine-like phase for the ISRS whereas a cosine-like describes the DECP. These criteria arise from the particular way of excitation: (*i*) in DECP case the photoexcited electron population produces a step-like change in the electron-ion potential configuration which will displace the lattice quasi-instantaneously and therefore the oscillation starts with a maximum; (*ii*) the ISRS shows a gradual increase of the phonon amplitude starting with t=0 which resembles a sines-like oscillatory motion. However, it was shown [66] that both mechanisms can be described in a more general theoretical framework that includes an excitation term based on two Raman tensors that have similar real components but different imaginary parts. The real part is related to the ISRS mechanism while the imaginary part with the displacive mechanism, and therefore DECP can be considered just a particular case of ISRS.

A simple way to describe the coherent phonon dynamics is to employ the equation of motion for a damped oscillator with different driving terms according to each excitation mechanism. Thus, one can write:

$$\mu^* \left(\frac{d^2Q}{dt^2} + \gamma \frac{dQ}{dt} + \Omega^2 Q \right) = F(t) \tag{2.15}$$

Here μ^* is the reduced mass of the system, Q is the coherent phonon amplitude with a frequency ω and a damping constant γ. The driving force is $F(t)$ that has the following expression for the stimulated Raman mechanism [16, 66]:

$$F(t) = \sum_{1,2} \chi_R^{(3)} E_1(t) E_2(t) = \sum_{1,2} \frac{\partial \chi^{(1)}}{\partial Q} E_1(t) E_2(t) \tag{2.16}$$

where $\chi_R^{(3)}$ is the Raman tensor given by the variation of susceptibility with the phonon
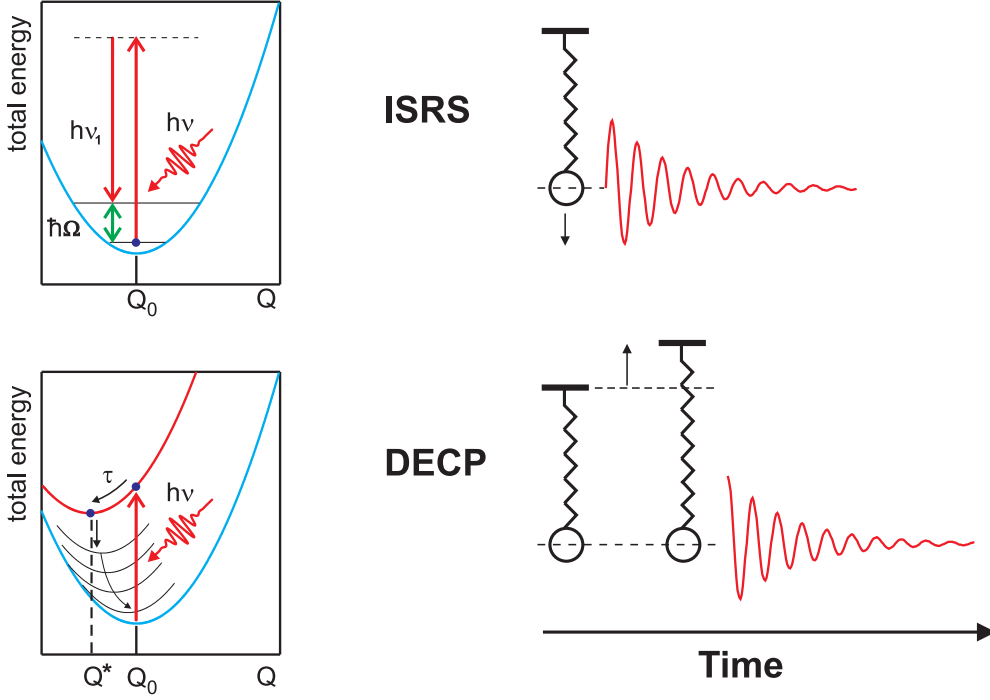
Figure 2.8: Comparison between the excitation mechanisms of coherent optical phonons. **Top**: the impulsive stimulated Raman scattering (ISRS). **Bottom**: displacive excitation of coherent phonons (DECP). On the left the excitation mechanisms are depicted in terms of potential energy surfaces (PES): for ISRS the excitation takes place in the ground state by emitting a phonon of energy $\hbar\Omega$ via inelastic Raman process whereas for DECP the laser promotes the system to an excited potential surface with a displaced lattice coordinate Q^* different from the ground state coordinate Q_0. The system evolves on the excited PES a time τ and starts to oscillate. After some time the vibrational potential is relaxed back to the ground state. On the right the corresponding oscillatory behavior for each type of excitation is displayed in the simple picture of the harmonic oscillator with the driving force shown by the arrow. The ISRS exhibits a sine-like oscillatory motion while the DECP a cosine-like one.

coordinate and E_1 with E_2 are the electric fields of the two photons involved in the Raman process. For the displacive mechanism, in the case of a semiconductor , the expression for the driving force has been deduced by Kuznetsov *et al.* [67] in the following form:

$$F(t) = 2\omega\sqrt{\frac{\hbar}{2\omega\rho V}}(C^v - C^c)N(t) \qquad (2.17)$$

where ρ is the reduced mass density and V is the volume, C^v and C^c are the deformational potentials for the valence and conduction bands, respectively, and $N(t)$ is the photoexcited electron population. From here one can see that the "initial kick" that launches the coherent phonon wavepacket is determined by the amount of excited carriers through $N(t)$ and, very important, the change of the electronic structure produced by lattice displacement *i.e.* electron-ion deformational potential.

Coherent phonon detection

One way to detect coherent phonons is to employ time-resolved optical methods that can resolve the small modulation in the refractive index of the system produced by lattice motion. This can be done in pump-probe measurements by detecting the relative changes in the linear reflectivity and/or transmissivity of the probe pulse, that appear after pump pulse excitation. In a similar manner, one can investigate phonon dynamics with optical second-harmonic generation *i.e.* a nonlinear optical method that gives information restricted to the surface/interface region due to symmetry considerations (see chapter 3). Thereby, phonon modes located at surfaces and even at buried interfaces can be detected [17, 68, 69]. Hence, employing simultaneously bulk and surface sensitive techniques *i.e.* linear reflectivity and SHG, respectively, one can distinguish between bulk and surface phonon modes, as was shown in [70].

A more direct way to visualize the coherent lattice dynamics is employing time-resolved x-ray diffraction [71], since this method gives access to phonon dynamics in a spatially and temporally resolved manner. This emerging field is under a continuous development in order to achieve a better temporal resolution [72].

The lattice vibrations at THz frequencies can be sources of electromagnetic radiation with a similar frequency. This has been demonstrated by Dekorsy *et al.* [73], they detecting the terahertz radiation emitted by coherent phonons in Te with time-resolved terahertz spectroscopy. There are a manifold of investigation methods that can not be remotely cited here but it is worth mentioning the multi-photon nonlinear ones, like coherent anti-Stokes Raman scattering (CARS) [74]. By choosing well-defined wavevectors of the involved photons one can produce tailor-made coherent phonons wavepackets with various q wavevectors.

At this point we close the discussion regarding the possible methods of investigation of coherent lattice dynamics and focus on the employed measurements tools in this work: the linear reflectivity and second harmonic generation. The basic questions to be answered are: (*i*) how to detect the modulation of the dielectric function of the material due to lattice vibration, (*ii*) what information can be retrieved from the transient signal *e.g.* in terms of excitation mechanism, (*iii*) can one get more insight about the available relaxation channels.

Let us start the discussion by looking at the figure 2.9 that shows the transient behavior of the SHG signal on the Gd(0001) surface as a function of pump-probe delay. Here one can immediately observe the well pronounced oscillations that are superimposed on a smoothly varying background. The former feature is ascribed [17] to a coherent optical phonon that oscillate at a frequency of 3 THz and the latter one to the transient relaxation of the excited electronic system via *e-e* and *e-p* scattering. Hence, the optical response of the system can be decomposed in different contributions that, in a first approximation, are proportional to the measured SHG signal and can be modelled as follows:

$$\Delta SHG \propto \chi_0^{(2)} + \frac{\partial \chi^{(2)}}{\partial T_e}\Delta T_e + \frac{\partial \chi^{(2)}}{\partial T_l}\Delta T_l + \frac{\partial \chi^{(2)}}{\partial Q}\Delta Q \qquad (2.18)$$

with $\chi_0^{(2)}$ is the susceptibility tensor for an unperturbed system and the other terms are the changes induced by the electronic temperature T_e, lattice temperature T_l and displaced
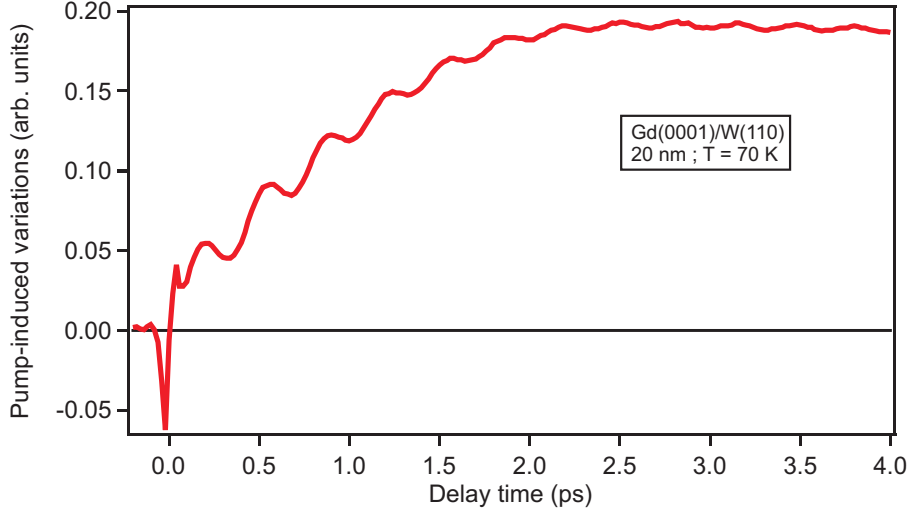
Figure 2.9: Time-resolved second harmonic response from Gd(0001) surface that shows the signature of the coherent optical phonon as the oscillatory component of the signal. This is superimposed on a smoothly varying background that describes the incoherent transient electron dynamics.

lattice coordinate Q, respectively.

A similar approach can be followed in order to retrieve the changes induced by coherent phonons in linear reflectivity of the sample:

$$\Delta R \propto R_0 + \frac{\partial R}{\partial \varepsilon}\frac{\partial \varepsilon}{\partial T_e}\Delta T_e + \frac{\partial R}{\partial \varepsilon}\frac{\partial \varepsilon}{\partial T_l}\Delta T_l + \frac{\partial R}{\partial \varepsilon}\frac{\partial \varepsilon}{\partial Q}\Delta Q \qquad (2.19)$$

where ε is the complex dielectric function of the system. After filtering out the incoherent background from the total signal, one ends-up with the pure oscillatory contribution and thus can identify the phase of the oscillation. In the above presented case of Gd(0001), the phase reveals a cosine-like behavior that points out to a displacive type of excitation.

2.4.2 Coherent phonon relaxation

Generally, the relaxation of a coherent phonon mode evolves via scattering events with the available incoherent population in the system that comprises thermal phonons, defects, electrons etc. In the case of ferromagnetic materials the coherent phonon mode can couple with excitations of the magnetic system *i.e.* magnons via phonon-magnon interaction. Depending on the involved scattering partners elastic and inelastic scattering events contribute to the relaxation of the coherent mode. Through elastic scattering the phase coherence is lost due to momentum randomization with no energy transfer, as is the case for scattering to defects [75]. Such a scattering process is known as *dephasing*. Inelastic scattering events involve changes in the momentum and energy among the scattering partners, this process being known as *decay/depopulation* or *energy relaxation*.

Thus we can evaluate the relaxation time of a coherent phonon mode according to Matthiessen's rule as the sum of the scattering rates determined by the total inelastic and
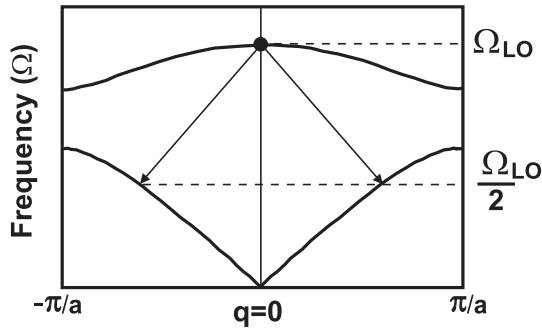
23

Figure 2.10: The anharmonic decay process in a generic phonon dispersion curves diagram, in which a zone center longitudinal optical (LO) phonon of energy $\hbar\Omega$ decays in two symmetric acoustical ones of energy $\hbar\Omega/2$ with the conservation of energy and momentum.

elastic scattering events that contribute:

$$\Gamma = \Gamma_e + \Gamma_i \qquad (2.20)$$

where $\Gamma = \tau^{-1}$ is inverse proportional with the lifetime time τ. In time-domain measurements one can determine τ as the characteristic decay time of the oscillatory components of the time-resolved signal.

In general the relaxation of the coherent optical phonons in semiconductors and semimetals [76, 77] is dominated by the inelastic scattering with thermal phonons. This phonon-phonon scattering or the *anharmonic decay* denotes (in the first approximation) the decay of a coherent optical phonon of energy $\hbar\Omega$ in two acoustical phonons with opposite wavevectors and energy $\hbar\Omega/2$. This process is illustrated in the figure 2.10 where a zone-center optical phonon decays in two symmetric acoustical phonons fulfilling the energy and momentum conservation. Depending on the details of the phonon dispersion curves also higher order anharmonic decay processes are possible that involves more phonons [76]. However, due to the strict momentum conservation condition these processes exhibit a lower probability.

In a first approximation, the phonon dynamics can be described in terms of the harmonic oscillator model. In reality the lattice potential is anharmonic (especially for the non-equilibrium conditions generated by the laser excitation) and higher order terms in lattice displacement should be accounted for. The phonon-phonon interaction or the anharmonic decay is determined by this anharmonicity of the lattice potential. For instance, the cubic anharmonic term gives rise to a three-phonon decay process, the fourth power term to a four-phonon process and so on.

In order to identify and disentangle the various decay channels one can modify some external parameters *e.g.* temperature, doping concentration (for semiconductors), defects density etc. This approach has been followed in the case of Bi [75], where the dephasing and energy relaxation time were separated by introducing various degrees of disordering produced by controlled ion implantation *i.e.* varying the dephasing rate.

Also varying the temperature of the system one can get information about the involved decay mechanisms. For example, the above mentioned cubic anharmonic decay gives a linear dependence of the decay rate Γ with temperature [76]. This can be quantified from experiment as [76, 64]:

$$\Gamma(T) = \Gamma_0 \cdot \left(1 + \frac{2}{exp(\frac{\hbar\Omega}{2k_B T}) - 1} \right) \qquad (2.21)$$

where Γ_0 is the anharmonic constant that gives the decay probability of the optical phonon of energy $\hbar\Omega$ in two acoustic phonons of energy $\hbar\Omega/2$, the latter being described by the Bose-Einstein function. The cubic (three-phonons) anharmonic decay can be also identified from the temperature-dependence of the coherent mode frequency: increasing the temperature a downwards shift in the frequency is expected [77].

The temperature behavior of the dephasing rate *i.e.* elastic scattering given *e.g.* by scattering with defects (impurity atoms), is considered to be temperature-independent. This is due to the low energy of the thermal phonons (generally a few tens of meV) that cannot excite internal atomic-like states (discrete, high-energy levels) of the impurity atoms.

For the case of metals, owing to the high density of the conduction electrons, the electron-coherent phonon scattering might play a role in the decay of coherent phonons. However, has been shown [64] for the case of Zn and Cd metals that the same phonon-phonon scattering mechanism plays the major role in the coherent phonon decay with a weak influence of the coherent phonon-electron scattering. This is not the case for the coherent phonons on the Gd(0001) metal surface, where the temperature-dependent study reveal an interesting behavior of the decay rate, being dominated by the scattering with electrons. These results are presented in detail in chapter 5.

2.5 Ultrafast magnetization dynamics

In this section we tackle another "hot" topic in the laser induced phenomena namely the femtosecond (de)magnetization dynamics on the ferromagnetic metals. The intention is to give a short overview of the relevant work done in the field and to present the actual understanding regarding the laser induced magnetization dynamics. This is meant to be a base for understanding of the results obtained on ferromagnetic Gd(0001), presented in chapter 5, that give a new approach concerning the ultrashort loss of magnetization following the femtosecond laser pulse excitation.

2.5.1 Earlier work

The first work reporting the demagnetization of a ferromagnetic Ni film after laser irradiation was by Agranat *et al.* [78]. Using variable laser pulse durations (between 5-20 ps and 40 ns) they concluded that demagnetization proceeds on a nanosecond time scale. Vaterlaus *et al.* employing time-resolved spin-polarized photoemission could show that spin relaxation time is approaching the picosecond range *i.e.* hundreds of picoseconds . They measured the magnetization behavior on Gd and Fe films using a 10 ns pump pulse and a probe pulse duration of 60 ps. The result was a spin relaxation time of 100 ± 80ps for gadolinium [79] while for iron a time scale ranging between 30 ps and 20 ns was deduced [80]. A theoretical input regarding the Gd results was provided by Huebner *et al.* [81]. According to their theory a spin relaxation time of 48 ps was computed, which was attributed to *spin-lattice relaxation* and was in a relatively good agreement with the experiment. These results lead to the conclusion that the demagnetization evolves via spin-lattice interaction and that the typical timescale resides somewhere in the hundreds of picosecond range.
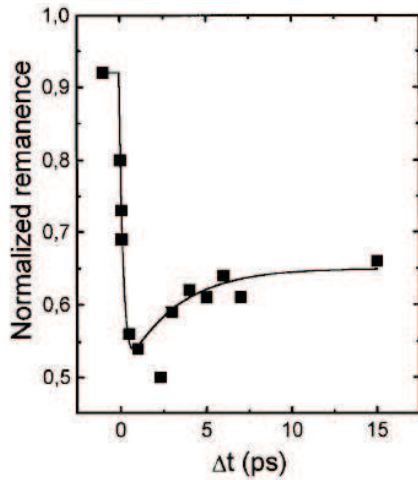
Figure 2.11: The key result of the work of Beaurepaire *et al.* [8] showing the behavior of the remanent MOKE signal for a 22 nm Ni film after laser excitation. The minimum in the transient MOKE signal, that is proportional with system's magnetization, is reached at about 2 ps.

In 1996 the group of Beaurepaire [8] came up with a surprising result for that time, namely a magnetization loss on a picosecond time scale *i.e.* orders of magnitude quicker as previously observed. They investigated Ni thin films with time resolution of 60 fs by employing pump-probe MOKE (magneto-optical Kerr effect)[12] measurements. The observed drop in the remanent MOKE signal (that is assumed to be proportional to the magnetization of the system) was reaching the lowest value around 2 ps. This important result is depicted in the figure 2.11. In order to explain this result a phenomenological three temperature model has been employed (*i.e.* electron, spin, and lattice temperatures) with the spin bath dynamics being delayed with respect to electron temperature formation. The observed demagnetization was attributed to an efficient electron-spin scattering process.

The work of Beaurepaire *et al.* initiated a new development of the field since their results were triggering a lot of interest in the community. Another important result was obtained by Hohlfeld *et al.* [9] by measuring the time-resolved nonlinear magneto-optical response of bulk Ni with second harmonic generation (SHG). They observed a quasi-instantaneous drop in magnetization within laser pulse duration (150 fs) employing various laser fluences. In this work, was demonstrated that after 280 fs, when the electronic system is thermalized, the transient magnetization depends on the electronic temperature in a classical Bloch's law dependence M(T) with $T = T_e$. This result is plotted in the figure 2.12. In the same year, the results of Scholl *et al.* [12] confirm the ultrashort drop in magnetization observed by Hohlfeld *et al.*. They measured ultrathin Ni films (6 Å and 12 Å thickness) with spin-resolved two-photon photoemission (SP-2PPE) and the main observation was that the transient magnetization evolves on two time scales: an initial, sudden magnetization drop on a 100 fs scale and a longer, smoother decrease on 500 ps scale. The former one was ascribed to demagnetization via excitation of Stoner pairs and the latter one to the phonon-magnon coupling. An improved version of the SHG work done by Hohlfeld *et al.* [9] was reported in [82] with a better time resolution of 40 fs and involving thin Ni and Co films grown under ultra-high vacuum (UHV) conditions [83, 84]. The conclusion was the same: instantaneous drop in magnetization within pulse duration and no delay between electron

---

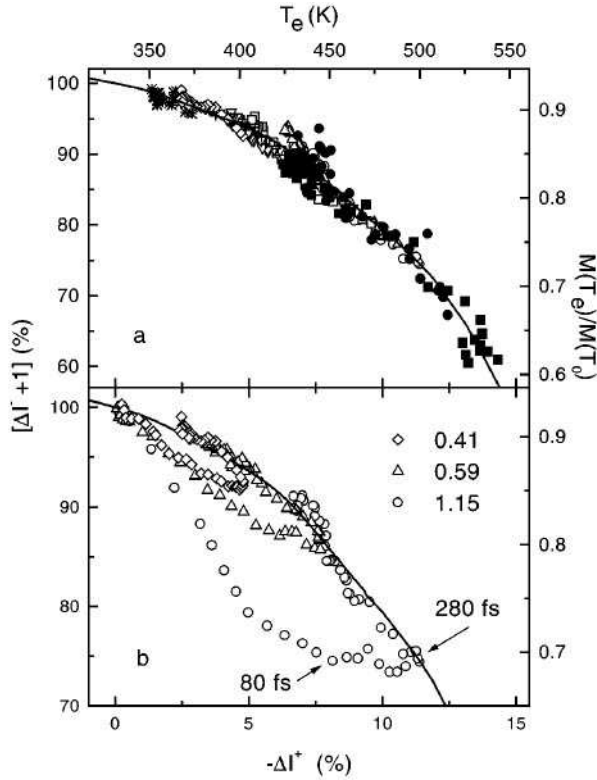[12]For details regarding the physics of MOKE please see chapter 3.

Figure 2.12: The magnetization dynamics as a function of electronic temperature measured on bulk Ni by Hohlfeld *et al.* [9] with time-resolved MSHG. The upper panel displays the values of transient magnetization (as measured by MSHG) at delays >300 fs for various pump fluences, which follow a $M(T_e)$ curve. The lower panel shows the measured data, at 280 fs and 80 fs delay time. For the 280 fs (electronic thermalization time) data the $M(T)$ behavior is reproduced whereas a consistent deviation is observed for the 80 fs delay.

and magnetization dynamics. Moreover, a total demagnetization of the thin ferromagnetic films (7 ML) was observed upon laser heating due to their reduced Curie point.

Some doubts about the quasi-instantaneous magnetization response after laser excitation were raised by Koopmans *et al.* [85] by ascribing their observed drop in the MOKE signal to artifacts determined by the state-filling or dichroic bleaching effects. In the same trend was the work of Regensburger *et al.* [86] who suggested that the observed pump-induced changes in the SHG response from Ni(110) surface does not reflect the magnetization dynamics at early times < 500 fs.

More recently [87, 88], from the dynamics of MOKE response measured on the $CoPt_3$ compound the authors concluded that, indeed, the ultrashort loss of MOKE signal on the first 100 fs time scale represents the magnetization behavior. Furthermore, they ascribed the spin dynamics on this compound to the 50 fs range *during* the thermalization of the electronic system [87].

Further insight in the laser-induced demagnetization dynamics can be obtained by monitoring the transient exchange-split electronic structure after excitation. Such a measurement has been performed by Rhie *et al.* [89] employing time-resolved photoemission spectroscopy on thin films (7 ML) of Ni/W(110). They reported a collapse of the exchange splitting of the $3d$ states on a time scale of ≈300 fs and a subsequent recovery with a ≈3 ps time constant. The invoked mechanism was electron-electron scattering with spin-flip mediated by the spin-orbit coupling for angular momentum conservation. One question that arises here is in how far one can consider the transient variation of the exchange split-

ting as reflecting the magnetization behavior, since Ni does not exhibit a pure Stoner-like behavior [90].

Recently [91] a linear magneto-optical study performed on various ferromagnetic insulator and metallic compounds showed again the existence of two time scales in photoinduced magnetization dynamics: an ultrashort one that has been ascribed to multiple emission of magnetic excitations, and a longer delay time scale that is material dependent and scales to magnetic anisotropy of the respective material.

From theory side an important input was provided by Zhang and Huebner [92, 93] in which they showed an accessible time range of 10 fs for magnetization dynamics on the transition metal Ni. This ultrashort time interval was obtained by taking into account the combined effect of spin-orbit coupling and the optical laser field. However, unrealistic high laser fields have been involved in the computation of these ultrashort time scales for demagnetization dynamics.

Very recently, Koopmans *et al.* [94, 95] have proposed a microscopic model where, in principle, the electron-phonon scattering with spin flip can be considered as an additional pathway responsible for demagnetization on the sub-picosecond time scale.

Summarizing the above presented works one can formulate a few conclusions that are emerging:

- there are two observed time scales on which magnetization evolves: upon laser excitation an ultrashort one within the first hundreds of fs and a slower one around few 100 ps;

- based on previous work the common agreement is that laser-induced demagnetization evolves on a sub-picosecond time scale (< 500 fs) but the elementary processes which are responsible are not unambiguously identified.

- the major question concerns the mechanism of transfer of angular momentum involved in the demagnetization process

- mostly transition metals and compounds were investigated using time-resolved MOKE, SHG and photoemission techniques;

- there is no systematic study of the same material involving complementary investigation techniques, that can access *e.g.* the magnetization and electronic structure simultaneously;

2.5.2 Laser-induced demagnetization

The demagnetization of a ferromagnetic sample is of fundamental interest for science and also of high relevance for applications in industry. There are several methods to demagnetize a piece of ferromagnetic material but here we will focus on the underlying physics of optically induced (de)magnetization dynamics. The interested reader is referred to the review works [1, 2] where different methods of manipulating magnetization on various time scales are presented.

We have seen earlier in this chapter that the optically injected energy by the laser pump pulse is redistributed and is relaxed mainly by electron-electron and subsequently
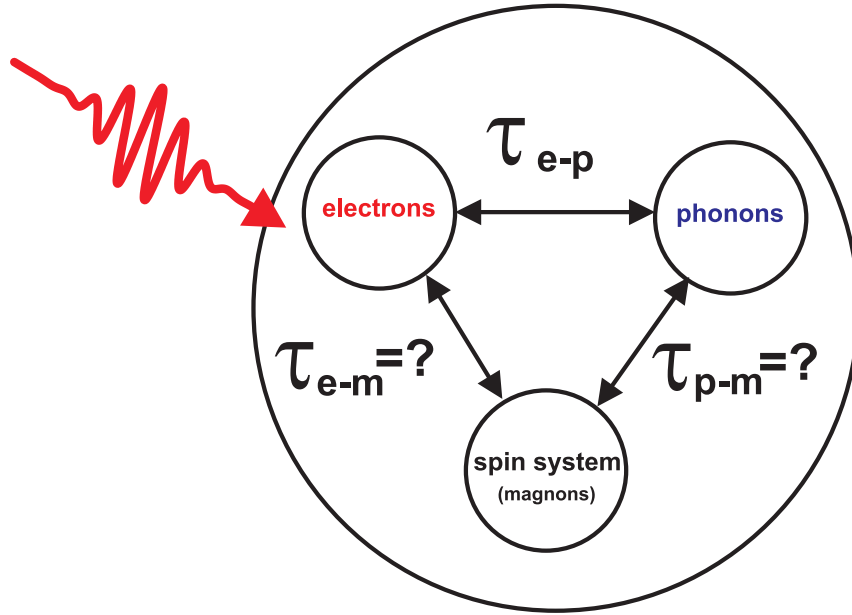
Figure 2.13: Illustration of the possible paths that can lead to demagnetization of a system after laser excitation. The laser pulse transfers the energy to the electron sub-system that can couple to the phonon or spin bath. The way in which the energy transfer take place among the quasi-particles *i.e.* either directly via electron-spin interaction or via electron-phonon and subsequently phonon-magnon coupling gives the characteristic time scale of demagnetization dynamics. A direct electron-magnon interaction favors a ultrafast loss of magnetization on a 100 fs range while an electron-phonon-magnon interaction sequence renders a 100 ps time interval for the demagnetization process. Note the necessity of angular momentum conservation for the involved interaction among quasiparticles baths.

electron-phonon scattering processes. Their characteristic time scales range from several hundreds of fs to several ps, respectively. On a longer time scale the energy relaxation is governed by thermal diffusion. Since there is an intrinsic relationship between electronic structure and magnetism, the question is to what extent is the latter one affected by the photoexcited electron population. Moreover, the presence of the magnetic ordering introduces another microscopic degree of freedom *i.e.* the spin bath to which the excited electrons can couple via electron-magnon interaction. Therefore, in order to investigate the ultrafast demagnetization one should account for the scattering events among electron, lattice and spin subsystems as well as for their coupling .

A possible scenario that can lead to demagnetization upon optical excitation of electronic system is presented in figure 2.13. The initially excited electron ensemble can couple directly to the spins (and/or excitation of the spin system *i.e.* magnons) via *e.g.* quasi-elastic spin-flip scattering. Alternatively, it might follow an indirect path where the deposited energy is transferred first to the lattice via *e-p* interaction and afterwards exciting the spin system via phonon-magnon coupling. The first mentioned demagnetization route has a purely electronic character and therefore a characteristic time scale for *e-e* interaction *i.e.* several 100 fs. For the latter one the energy flow involves an intermediate

energetic sink, the phonon bath, and therefore this process would take place on a slower picosecond time scale, that is less likely to explain a 100 fs magnetization loss. Thus, for a comprehensive understanding of the laser-induced demagnetization process one has to address several issues such as:

- to identify and disentangle the elementary spin scattering mechanisms and their relevant timescales

- to identify the processes which ensure the conservation of angular momentum on the ultrafast time scale

One of the microscopic mechanisms that can mediate the laser-induced demagnetization is the spin-orbit coupling. Upon laser irradiation the electronic system is excited. Since the light can access just the orbital part of the electronic wavefunction there is no direct light-induced spin-flip. Assuming a strong spin-orbit interaction, there will be a net momentum transfer from orbit to the spins, which disturb the last ones from equilibrium and start to fluctuate. Average spin fluctuations are equivalent to a decrease in magnetization. The spin-orbit strength gives the time scale on which this demagnetization scenario evolves. More accurately, the spin-orbit interaction that can mediate electronic spin-flip scattering events can be express under the following hamiltonian:

$$H_{so} = \lambda \mathbf{L} \cdot \mathbf{S} = \lambda[\mathbf{L}_z \cdot \mathbf{S}_z + \frac{1}{2}(\mathbf{L}^+ \cdot \mathbf{S}^- + \mathbf{L}^- \cdot \mathbf{S}^+)] \tag{2.22}$$

where $\mathbf{L}$ and $\mathbf{S}$ are the the orbital and spin moment operators and λ is the spin-orbit coupling strength. The spin-flip event is given in terms of annihilation and creation spin moment operators. One can see that any change in the spin moment $\mathbf{S}^-$ *e.g.* spin flip is balanced by a corresponding reaction in the orbital moment $\mathbf{L}^+$ and vice-versa. The probability of such a process is determined by the strength of the spin-orbit coupling λ. The quantization axis of the system, given by magnetization direction, is along z direction.

But what is happening in systems with a weak or vanishingly small spin-orbit interaction, like Gd(0001)? Is the demagnetization process slower? Or there is another microscopic mechanism involved? These questions will be addressed in the chapter 5 of this thesis.

Another way of thinking at the photoinduced ultrafast demagnetization process is by starting from the picture of the finite-temperature magnetization in equilibrium conditions. Depending on the type of the ferromagnet, *i.e.* itinerant or localized moment, there are two opposite models, Stoner and spin-mixing (see section 2.1), that describe the magnetization state under the effect of thermal excitations *i.e.* temperature. In the spin-mixing picture the magnetization is decreased by excitations (magnons emission) or fluctuations of the localized magnetic moments accompanied by a constant exchange-split electronic structure whereas in the Stoner model the magnetization at elevated temperatures is decreased by spin-flip scattering between bands with opposite spin orientation accompanied by a decreased exchange splitting that vanishes above T_C. Thus, it will be interesting to monitor these two quantities, the magnetization or the local spin polarization and the exchange splitting on an ultrafast timescale upon laser excitation. This approach

has been followed in this work on the localized magnetic moment ferromagnet Gd, using the complementary information given by time-resolved nonlinear magneto-optics and photoemission spectroscopy.

Summarizing this section, it is still unclear which of the above mentioned demagnetization mechanisms governs the nature of photoinduced magnetization dynamics. Whether is the spin-flip scattering, the emission/absorption of quasiparticles like magnons or phonons, the effect of non-equilibrium electron dynamics, the exchange interaction or the interplay between spin-orbit coupling and laser field is still to be investigated. The contribution of the present work relies on laser-induced spin dynamics on the localized-moment ferromagnet Gd and propose a novel demagnetization mechanism on an ultrashort timescale of 100 fs and faster. This "femtomagnetism" behavior will be detailed in chapter 5.